One-Nanometer-Thick Interfaces of Titania Nanosheets for Reversible Zn-Metal Electrodes

Chenhui Wang, Nobuyuki Sakai*, Yasuo Ebina, Daiming Tang, Renzhi Ma, Takayoshi Sasaki*

Research Center for Materials Nanoarchitectonics (MANA), National Institute for Materials Science (NIMS), Namiki 1-1, Tsukuba, Ibaraki 305-0044, Japan

* Corresponding author, E-mail: SASAKI.Takayoshi@nims.go.jp, SAKAI.Nobuyuki@nims.go.jp

ABSTRACT: Zinc-based aqueous energy storage technology has sparked widespread interest because of its low cost, high energy density, high safety, and environmentally benign manufacturing process. However, progress has been severely impeded by H_2 evolution and Zn dendrite formation. Interface engineering is a promising avenue for addressing these issues. Herein, molecularly thin $Ti_{0.87}O_2$ nanosheets were deposited on a Zn electrode surface via spin coating to form a monolayer film with a thickness of ~1 nm. The electrode surface was fully covered with neatly tiled $Ti_{0.87}O_2$ nanosheets and thus effectively suppressed the H_2 evolution side reaction and reduced the Zn nucleation potential, resulting in uniform electrochemical deposition and reversible plating/stripping of Zn. As a consequence, the cycle life was drastically improved from 105 to over 1400 h at 1 mA cm^{-2}/1 mAh cm^{-2}. This study has established an economical and efficient molecular-scale interfacial engineering strategy enabling practical applications of Zn metal electrodes, and it also shows great promise for use with other metal electrodes in Li, Na, Al, and Mg metal batteries.

Energy storage technology has played an important role in improving the environment and the quality of human lives because it provides electricity and allows the use of electrical devices anywhere and anytime, significantly promoting the utilization of renewable energy.[1-4] Due to the abundant reserves, low cost, high stability, and high specific capacity (5855 mAh cm^{-3} or 823 mAh g^{-1}), zinc-based energy storage technology has attracted wide attention and shown promise for application in portable electronics, electric vehicles, and large-scale energy storage.[5-7] However, Zn dendrite growth, Zn corrosion, and the H_2 evolution side reaction are the intractable challenges that hinder practical development.[8,9] Nonuniform Zn plating/stripping results in protrusions, which may pierce a separator and cause a short circuit. These protrusions may also fall off from the substrate to form "dead zinc", reducing the amount of the active material because of the small contact area and weak adhesion. Moreover, side reactions, such as Zn electrochemical corrosion and H_2 evolution, lower the energy efficiency substantially. In addition, these reactions produce passivation layers or massive amounts of gas, reducing the kinetics and reversibility of the zinc electrode. Furthermore, battery expansion and even cracking may occur.

Various strategies, such as electrolyte additives,[10,11] separator modification,[12,13] design of a 3D porous structure[14,15] or alloy,[16] and interfacial engineering,[17,18] have been applied to address these problems. Among these, interfacial engineering is the most promising. It directly controls the interfacial state for Zn plating/stripping reactions, thereby accelerating the reaction kinetics, suppressing side reactions, and homogenizing the ion distribution and electric fields.[19] Thus, it may improve the morphology of deposited Zn and current efficiency, leading to a dendrite-free electrode with high cycling stability. A variety of interface layers have been fabricated using a wide range of materials, including inorganic materials such as $CaCO_3$,[20] TiO_2,[21] ZrO_2,[22] $NaTi_2(PO_4)_3$,[23] montmorillonite,[24] and ZnSe;[25] organic polymers such as poly(vinyl butyral)[26] and polyamide;[27] and inorganic–organic hybrids.[28-32] These interfaces function as either physical separators to suppress side reactions by avoiding direct contact between Zn and the electrolyte or as controllers to adjust the transport, distribution, and interaction of ions/electrons, leading to uniform deposition of Zn with high efficiency and stability. However, the majority of interfacial layers have a micrometer-scale thickness, resulting in a high proportion of inactive materials and a long migration distance for electrons and ions, which significantly reduce the specific capacity and increase the cost and resistance. Recently, thinner interfacial layers have been fabricated through atomic/molecular layer deposition,[33] but the need for a costly facility and the limited number of applicable materials make this technique unfavorable. Thus, it is of considerable importance to develop ultrathin interfaces for Zn electrodes via a simple and versatile method. In particular, an interfacial layer with a molecular-scale thickness would

allow for sophisticated engineering and ultimate performance.

Two-dimensional (2D) materials, which are characterized by their molecular thinness and large aspect ratios, have been important targets in materials science in recent decades, and promising applications have been proposed in a wide range of fields, such as optics,[34,35] electronics,[36] thermotics,[37,38] and magnetics.[39,40] In particular, 2D metal oxide nanosheets are versatile functional blocks that exhibit outstanding potential for constructing advanced materials and devices, including ultrathin film electronics.[41-45] They have "organic-material-like" solution processability in addition to robust inorganic stability. These 2D oxide nanosheets are monodispersed in liquids and thus can be assembled into a variety of nanostructured films on various substrates by simple solution-based methods, such as the Langmuir–Blodgett process (LB),[46,47] layer-by-layer assembly (LBL),[48-50] spin coating,[51-53] and droplet assembly.[54] More importantly, the film thickness can be controlled stepwise at the molecular level (1-2 nm), while the coating area can cover square centimeters or more. Thus, we can expect high feasibility and application potential in fabricating molecularly thin interfacial layers for zinc electrodes based on the above-mentioned materials and methods to achieve advanced zinc-based energy storage systems. Nevertheless, such studies have not yet been reported.

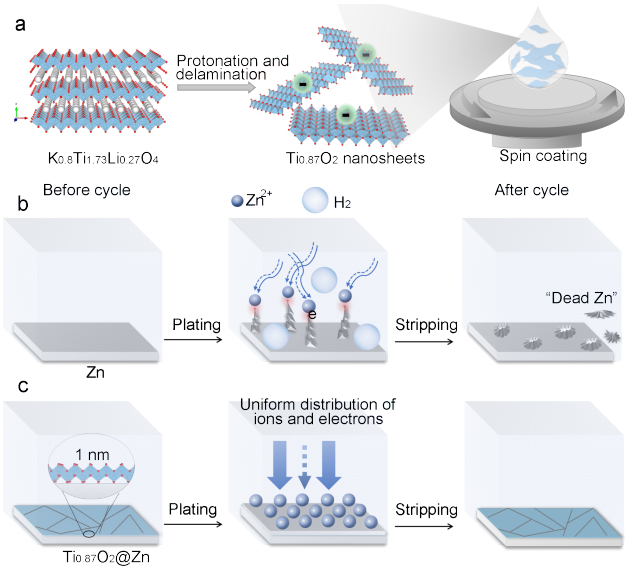

Scheme 1. (a) Schematic illustration for fabrication of a zinc electrode covered with a monolayer film of neatly tiled $Ti_{0.87}O_2$ nanosheets.[55] Schematic illustrations of plating/stripping processes of (b) a bare zinc electrode (Zn) and (c) a zinc electrode covered with a monolayer film of $Ti_{0.87}O_2$ nanosheets ($Ti_{0.87}O_2$@Zn) in aqueous electrolyte for use in a zinc-based energy storage system.

Although TiO_2 coating has been verified to act as an effective protecting layer for Zn electrodes due to its highly stable and insulating nature,[21] the TiO_2 layers are rather thick, which would largely reduce the specific capacity of the Zn electrodes. In this study, we employ unilamellar 2D titania nanosheets of $Ti_{0.87}O_2$ because we can precisely design the ultrathin coating layer at a step of ~1 nm, corresponding to the nanosheet thickness. As a proof-of-concept, a 1 nm-thick and centimeter-wide interface comprising $Ti_{0.87}O_2$ nanosheets was fabricated on the Zn metal electrode via spin coating, expecting excellent stability and reversibility for Zn-based energy storage devices. Micrometer-sized unilamellar $Ti_{0.87}O_2$ nanosheets, which were obtained by delaminating a layered titanate,[56-58] were deposited as a monolayer film on the Zn electrode surface. Upon spin coating of the nanosheet suspension under optimized conditions, $Ti_{0.87}O_2$ nanosheets were neatly packed into a centimeter-sized monolayer film intimately bound to the substrate. This thin interface, with its molecular-level thickness, preserved the electrical conductivity and specific capacity of the Zn electrode while considerably enhancing stability and reversibility. Because of the high stabilities and negatively charged surfaces of $Ti_{0.87}O_2$ nanosheets, they serve not only as protective layers to prevent direct contact between Zn and the electrolyte but also as efficient Zn^{2+} enrichers and distributors to supply sufficient and uniform sites, leading to a dendrite-free and reversible Zn electrode with high stability and current efficiency. As a result, the Zn electrode with a 1-nm thick interface of $Ti_{0.87}O_2$ nanosheets significantly suppressed side reactions while greatly enhancing the cycling performance from 105 to over 1400 h at 1 mA cm^{-2}/1 mAh cm^{-2}, showing the applicability of this strategy.

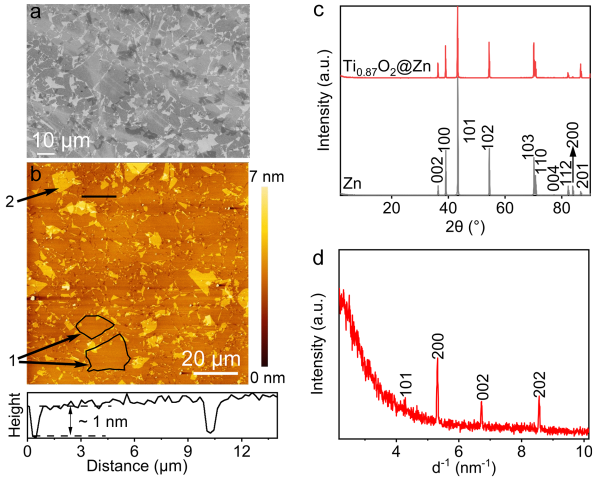

Figure 1. (a) SEM image of $Ti_{0.87}O_2$@Zn. (b) AFM image and height profile along the black line of $Ti_{0.87}O_2$@Si (monolayer and overlapped nanosheets (outlined) are indicated by 1 and 2, respectively). (c) XRD data of Zn and $Ti_{0.87}O_2$@Zn. (d) In-plane XRD pattern of $Ti_{0.87}O_2$@Si.

Unilamellar $Ti_{0.87}O_2$ nanosheets were prepared by exfoliating the layered titanate precursor $K_{0.8}Ti_{1.73}Li_{0.27}O_4$ through a soft-chemical exfoliation process (Scheme 1a). As shown in Figure S1, X-ray diffraction (XRD) data for $K_{0.8}Ti_{1.73}Li_{0.27}O_4$ and its acid-form, $H_{1.07}Ti_{1.73}O_4{\cdot}H_2O$, indicated orthorhombic lepidocrocite-related structures, consistent with reported results.[56-58] Scanning electron microscopy (SEM) images exhibited a platy morphology with particle sizes of tens of micrometers (Figure S2, S3). Reaction with an aqueous tetrabutylammonium (TBA) hydroxide solution promoted delamination into colloidal single layers (Figure S4a). Images produced with atomic force

microscopy (AFM) after drying the suspension on a Si plate showed micrometer-sized 2D nanosheets. The unique thickness of 1.2 nm indicated the unilamellar nature.[59] The suspension of $Ti_{0.87}O_2$ nanosheets dispersed in dimethyl sulfoxide (DMSO) was prepared by recovering the nanosheets from the aqueous suspension by high-speed centrifugation, followed by redispersion in DMSO. The nanosheet content was adjusted to 0.1 wt% for film fabrication. The Zn substrate used as an electrode showed a smooth surface except for some pits (Figure S5). The rotation speed of the spin coating process was optimized to achieve full coverage with the monolayer film.[53] Higher rotation speeds of 1400 and 2000 rpm left the central region of the zinc substrates uncovered (Figure S6a and b). In contrast, coating at 1200 rpm was found to produce a uniform and intact film fully covering the area of the centimeter-scale substrate (Figure S6c). As shown in Figure 1a, $Ti_{0.87}O_2$ nanosheets with sizes of several to tens of micrometers were well packed side by side with leaving small gaps between them. This neat tiling was also visualized by AFM (Figure 1b), confirming the formation of a flat, dense, and intact film with a thickness of 1 nm. On the basis of the analysis of height histogram (Figure S7), the areas of monolayer and bilayer regions were estimated to be 85.2% and 14.8%, respectively, and the amount of the $Ti_{0.87}O_2$ nanosheets on the substrate is 1.15 times the amount for complete coverage with the $Ti_{0.87}O_2$ nanosheets in a monolayer. The mass of the $Ti_{0.87}O_2$ nanosheet per area is calculated as 2.2×10^{-4} mg/cm^2 on the basis of the 2D rectangular unit cell (0.3760 nm × 0.2976 nm) which contains two formula units of $Ti_{0.87}O_2$.[50] Hence, the mass loading of the $Ti_{0.87}O_2$ nanosheets was estimated as 2.5×10^{-4} mg/cm^2. Various substrates, such as zinc sheets (Zn), silicon wafers (Si), and stainless steel (SS), were employed for various characterizations and electrochemical tests, and their surfaces were successfully covered with monolayer films of neatly tiled $Ti_{0.87}O_2$ nanosheets. They are named $Ti_{0.87}O_2$@substrate ($Ti_{0.87}O_2$@Zn, $Ti_{0.87}O_2$@Si, and $Ti_{0.87}O_2$@SS).

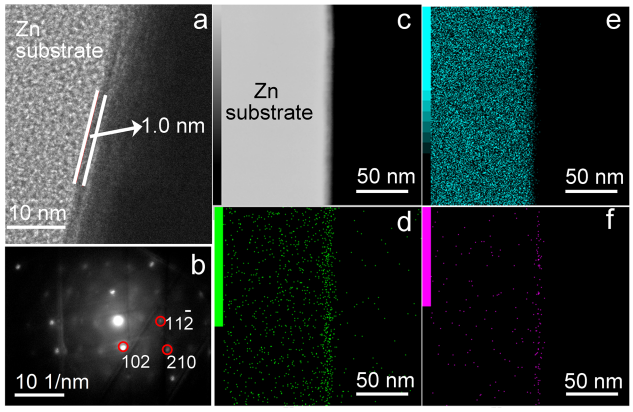

Figure 2. (a) TEM image of the cross-sectional profile of $Ti_{0.87}O_2$@Zn. (b) Electron diffraction pattern of a Zn area in $Ti_{0.87}O_2$@Zn. (c) STEM image and EDS mapping of the cross-section for $Ti_{0.87}O_2$@Zn: (d) O, (e) Zn, and (f) Ti.

The XRD pattern shown for Zn in Figure 1c was consistent with Zn metal exhibiting a hexagonal structure. No new peak appeared after a single spin-coating (red line in Figure 1c), while repeated spin-coating processes gave rise to a new peak at 5°. This peak showing an interlayer spacing of 1.5 nm can be attributed to the restacked $Ti_{0.87}O_2$ nanosheets accommodating TBA^+, and its intensity increased with increasing spin-coating cycles (Figure S8).[51] These results demonstrated that the nanosheets were deposited layer-by-layer upon repeating the spin-coating process, which is consistent with our previous reports.[51,52] The in-plane XRD technique could not be applied to $Ti_{0.87}O_2$@Zn because the surface was not sufficiently flat. Instead, after one spin-coating, the sample on Si (Figure 1d) exhibited sharp peaks, which were indexed as the 2D rectangular lattice of $Ti_{0.87}O_2$ nanosheets with unit cell dimensions of a = 0.3760 nm and c = 0.2976 nm, supporting the presence of $Ti_{0.87}O_2$ nanosheets on the substrate surface. The interface structure of $Ti_{0.87}O_2$@Zn was characterized with scanning transmission electron microscopy (STEM), transmission electron microscopy (TEM), and energy-dispersive X-ray spectroscopy (EDS). The nanosheets with a thickness of 1 nm and bound to the substrate were clearly resolved (Figure 2a). The selected-area electron diffraction pattern from the substrate (the area on the left side of Figure 2a) was consistent with Zn metal exhibiting a hexagonal structure (Figure 2b). EDS mapping revealed a uniform distribution of Zn in the area corresponding to the Zn substrate and a thin layer of the elements of the O and Ti on top of the Zn substrate (Figure 2c-f). These results confirmed the presence of a monolayer film of $Ti_{0.87}O_2$ nanosheets on the Zn substrate.

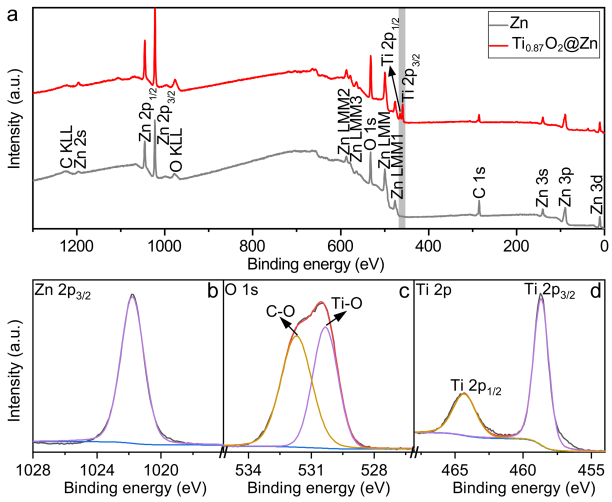

Figure 3. (a) XPS survey spectra of Zn and $Ti_{0.87}O_2$@Zn surfaces. High-resolution (b) Zn $2p_{3/2}$, (c) O 1s, and (d) Ti 2p XPS spectra for $Ti_{0.87}O_2$@Zn.

The compositions and surface chemical states of the Zn substrates with and without the coating layer were examined by X-ray photoelectron spectroscopy (XPS). The Zn substrate displayed signals for Zn, C, and O (Figure 3a), while $Ti_{0.87}O_2$@Zn gave a Ti signal in addition to those for the above three elements. The signal from Zn was not significantly reduced after coating with the $Ti_{0.87}O_2$ nanosheets, consistent with coverage by an ultrathin $Ti_{0.87}O_2$ layer on the Zn substrate. The peak observed at 1021.8 eV was ascribed to the Zn $2p_{3/2}$ binding energy, indicating the metallic state of Zn in the $Ti_{0.87}O_2$@Zn sub-

strate (Figure 3b). The high-resolution O 1s spectrum was deconvoluted into two peaks at 531.7 and 530.3 eV, which were attributable to C–O and Ti–O bonds, respectively (Figure 3c). The peaks at 464.3 and 458.7 eV were due to the Ti $2p_{1/2}$ and Ti $2p_{3/2}$ binding energies of Ti–O, verifying the presence of tetravalent titanium in the nanosheets (Figure 3d).

$Ti_{0.87}O_2$@Zn was further examined by time-of-flight secondary-ion mass spectrometry (TOF-SIMS), which is characterized by superhigh sensitivity and small detection depths of ~1-2 nm. As shown in Figure 4a, the Zn and Ti species were detected in the TOF-SIMS spectrum. The intensity of the Ti signal was much higher than that of the Zn signal, which should be due to monolayer coverage of the Zn electrode with $Ti_{0.87}O_2$ nanosheets (Figure 4b-d). Mapping of these positive ions verified the homogeneous distributions of the Zn and Ti species, suggesting the presence of uniform and intact $Ti_{0.87}O_2$ interfaces on the Zn substrate (Figure 4e-g).

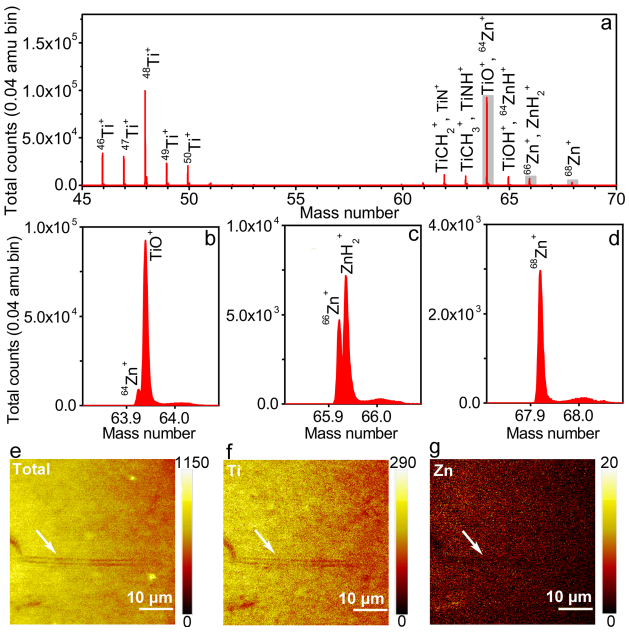

Figure 4. (a) TOF-SIMS spectrum and the enlarged spectra for $Ti_{0.87}O_2$@Zn with mass numbers of (b) 64, (c) 66, and (d) 68 in the positive mode. Distributions of fragment positive ions of (e) all, (f) Ti, and (g) Zn ions on $Ti_{0.87}O_2$@Zn. The lines (shown by arrows) in the images (e-g) are scratches possibly formed during sample preparation.

The effect of this monolayer $Ti_{0.87}O_2$ film on Zn plating and stripping performance was examined with galvanostatic charge/discharge tests. As shown in Figure 5a, Zn/Zn and $Ti_{0.87}O_2$@Zn/$Ti_{0.87}O_2$@Zn symmetric batteries were charged and discharged at different current densities. With increasing current density, the voltage hysteresis, or the potential difference between charge and discharge, increased, which indicated increasing polarization due to Zn plating and stripping in these two symmetric batteries. The $Ti_{0.87}O_2$@Zn/$Ti_{0.87}O_2$@Zn battery worked well at all current densities from 0.5 mA cm^{-2} to 10 mA cm^{-2} and upon return to 0.5 mA cm^{-2}. In contrast, the Zn/Zn battery short-circuited before accomplishing all of the steps, indicating that the Zn electrodes suffered severely from dendrite growth, especially upon cycling at larger current densities. Note that the $Ti_{0.87}O_2$ nanosheets as well as the TBA^+ ions adsorbed on them are electrochemically inert in the potential range observed.[60] The galvanostatic charge/discharge cycling stabilities of Zn electrodes and $Ti_{0.87}O_2$@Zn electrodes were also tested at 1 mA cm^{-2} through all of the cycles. As shown in Figures 5b and S9, the Zn/Zn battery short-circuited after cycling for 105 h, while the $Ti_{0.87}O_2$@Zn/$Ti_{0.87}O_2$@Zn battery worked well for more than 1400 h without a short circuit. During the cycling for 1400 h, the number of electrons (2.52×10^3 C cm^{-2}) passed across the electrode surface for the deposition of Zn is >1.9 × 10^6 times larger than that is necessary if four-electron reduction of the $Ti_{0.87}O_2$ nanosheets (1.31×10^{-3} C cm^{-2}) is assumed. Since the electrodes showed the cycle performance without a short circuit even after such a large number of electrons flowed, it is inferred that the nanosheet is intact during the cycle. The cycling stability time was improved over 13-fold by covering the electrode with the unilamellar $Ti_{0.87}O_2$ nanosheets, which surpassed most of interfaces reported with much larger thicknesses for Zn electrodes (Table S1). The voltage hysteresis was decreased for both the Zn/Zn and $Ti_{0.87}O_2$@Zn/$Ti_{0.87}O_2$@Zn batteries over the initial several cycles, indicating decreases in battery polarization (Figure S9a). Compared with the Zn/Zn battery, the $Ti_{0.87}O_2$@Zn/$Ti_{0.87}O_2$@Zn battery showed a smaller voltage hysteresis, which reached a stable value as low as 67 mV and was maintained until 1400 h (Figure S9b, c). As shown in Figure 5c, uneven Zn dendrites (marked with red ellipses) were obviously formed on the surfaces of the Zn electrodes. In addition, the uneven Zn dendrites were intersected with the glass fibers peeled from the separator (indicated by blue arrows), suggesting the penetration of Zn that finally causes a short circuit. In contrast, the surface of the $Ti_{0.87}O_2$@Zn electrode after cycling showed a smoother morphology (Figure 5d). The thickness of the deposited Zn layer is estimated to be 1.7 μm at the maximum under the present charge/discharge conditions (1 mAh cm^{-2}), by assuming that all of the electrons are used for the two-electron reduction of Zn^{2+} into the deposition of Zn (density: 7.14 g cm^{-3}). Stable repetition of the plating/stripping processes of this large amount of Zn may indicate that Zn is deposited on or above the $Ti_{0.87}O_2$ layer, which is empirically supported by the XPS data that the Ti signal for the $Ti_{0.87}O_2$@Zn became negligible after Zn deposition (Figure S10). The deposition of Zn may start on the Zn substrate exposed to the electrolyte in the gaps between the nanosheets and laterally grow to cover the nanosheet, which is suggested by the preferential enhancement of the 002 peak in the XRD data (Figure S11). These results demonstrated the positive effects of the Zn electrode coverage with $Ti_{0.87}O_2$ nanosheets. We also examined the charge/discharge curves for the Zn electrodes coated with 2- and 5-layer nanosheet films (Figures S12-S13). The resistivity of the Zn substrates hardly increased with increasing the number of the $Ti_{0.87}O_2$ nanosheet layers (Table S2). Their cycling stabilities were also improved compared to the bare Zn electrodes, whereas the lifetime declined with an increase in the layer number of nanosheets. As the number of $Ti_{0.87}O_2$ nanosheet layers increases and the abundance of exposed Zn sub-

strate decreases, a part of the deposited Zn may remain on the nanosheets during the stripping process, which causes uneven deposition of Zn, leading to the formation of Zn dendrite. Hence, the monolayer coverage is the best of choice for the reversible Zn electrodes.

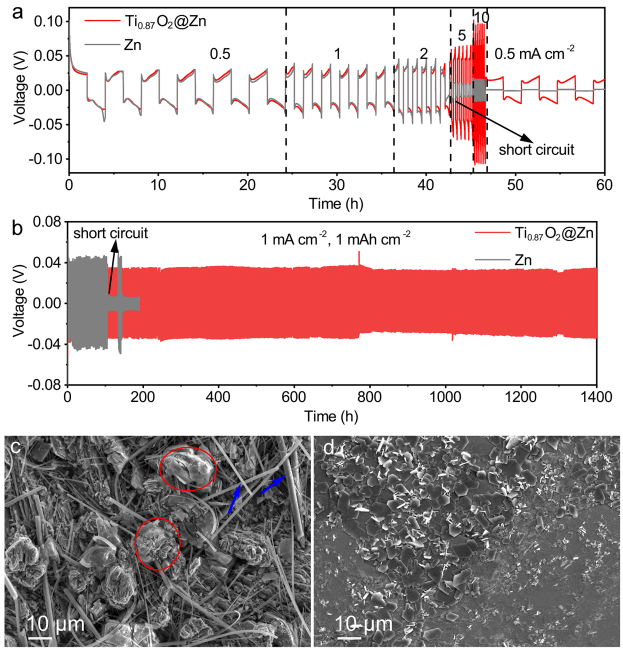

Figure 5. (a) Galvanostatic charge/discharge curves for Zn/Zn and $Ti_{0.87}O_2$@Zn/$Ti_{0.87}O_2$@Zn symmetric batteries at different current densities. (b) Long cycling tests at a current density of 1 mA cm^{-2} and capacity of 1 mAh cm^{-2}. SEM images of (c) Zn and (d) $Ti_{0.87}O_2$@Zn electrodes after charge/discharge cycles run for 105 and 1400 h, respectively.

The physicochemical and electrochemical properties of $Ti_{0.87}O_2$@Zn electrodes were studied to explore the underlying mechanism. The zeta potential of the $Ti_{0.87}O_2$ suspension was −27 mV (Figure S14), indicating negative charges on the $Ti_{0.87}O_2$ nanosheets. This colloid undergoes flocculation upon in contact with the $ZnSO_4$ solution, which is commonly used as the electrolyte of zinc-ion batteries; this reaction is promoted by restacking $Ti_{0.87}O_2$ nanosheets, accommodating Zn^{2+} between them via the electrostatic attraction (Figure S4b). Elemental analysis of the flocculated product recovered indicated the uptake of ~0.49 Zn^{2+} per formula weight of $Ti_{0.87}O_2$ nanosheets. On the structural consideration, this composition corresponds to approximately one Zn^{2+} ion per one 2D unit cell area (indicated above) of nanosheet. These data indicate that the monolayer $Ti_{0.87}O_2$ film can attract Zn^{2+} ions near the electrode at a high density comparable to that of the basal plane of the Zn crystal, which contributes to a uniform Zn^{2+} distribution on the surface.

The hydrophilic nature of the electrode was also examined because it affects the electrochemical performance in an aqueous electrolyte. As shown in Figure S15a, a water droplet on the Zn surface showed a hemispherical shape with a contact angle of 90°, suggesting low surface hydrophilicity. In contrast, a water droplet spread out on the $Ti_{0.87}O_2$@Zn surface with a contact angle of 4.5°, indicating that the monolayer $Ti_{0.87}O_2$ film improved the electrode hydrophilicity (Figure S15b). The higher hydrophilicity may be ascribed to formation of hydrogen bonds between $Ti_{0.87}O_2$ and H_2O, contributing to good contact between the electrode and electrolytes as well as a reduction in the ohmic polarization of the electrode.[61,62]

The current efficiency for Zn plating can be substantially reduced by H_2 evolution via the main side reaction. Evolved H_2 bubbles are adsorbed on the electrode surface, blocking active sites and promoting the formation of loosely bound or dead Zn. In addition, H_2 gas accumulated and encapsulated in the cell during cycling could break the cell and cause malfunction. Then, the effect of monolayer coverage with the $Ti_{0.87}O_2$ nanosheets on the suppression of H_2 evolution during Zn plating was examined by linear sweep voltammetry (LSV). The LSV curves measured in the Na_2SO_4 electrolyte only reflected the H_2 evolution reaction, while the combined reactions of H_2 evolution and Zn plating can be monitored in the $ZnSO_4$ electrolyte. In the Na_2SO_4 electrolyte, the Zn electrode showed a current density larger than that of the $Ti_{0.87}O_2$@Zn electrode at −1.2 to −1.9 V, indicating higher H_2 evolution activity (Figure S16a). In addition, a nonsmooth curve profile with occasional spikes for the Zn electrodes may be associated with violent gas evolution. In the $ZnSO_4$ electrolyte, the Zn and $Ti_{0.87}O_2$@Zn electrodes showed similar current densities, indicating similar activities for the combined Zn plating and H_2 evolution processes (Figure S16b). Accordingly, these results indicated that the $Ti_{0.87}O_2$@Zn electrode had a higher Zn plating reaction activity and a lower H_2 evolution side reaction activity than the Zn electrode. Specifically, monolayer coverage of the Zn electrode with unilamellar $Ti_{0.87}O_2$ nanosheets promoted Zn plating and suppressed H_2 evolution. Preferential adsorption of Zn^{2+} as opposed to that of H^+ on the $Ti_{0.87}O_2$ nanosheets may contribute to this behavior.

Since Zn nucleation is the initial and essential step for the Zn plating process, Zn nucleation on stainless steel (SS) and $Ti_{0.87}O_2$@SS was monitored by the galvanostatic current technique. As shown in Figure S17, the nucleation overpotential corresponded to a difference between the tip and the platform potentials. The nucleation overpotential of $Ti_{0.87}O_2$@SS was smaller than that of SS, proving that monolayer coverage with unilamellar $Ti_{0.87}O_2$ nanosheets promoted the effective nucleation of Zn. These results strongly suggest that the monolayer $Ti_{0.87}O_2$ film efficiently reduced the electrochemical polarization of the Zn electrode. Evolution in the morphology of Zn deposited on the electrodes was monitored in situ with an optical microscope in a homemade setup (Figure S18). As shown in Movie S1, a large difference in brightness was observed for the surface of the Zn electrode after deposition, indicating that the deposition rate on the surface of the Zn electrode was locally dependent. These local fluctuations could eventually develop dendrites. Compared with the bare Zn electrode, the surface of the $Ti_{0.87}O_2$@Zn electrode after deposition was much more uniform, suggesting suppression of Zn dendrite formation (Movie S2). These results have proven that monolayer coverage with unilamellar $Ti_{0.87}O_2$ nanosheets effectively suppressed electrode polarization,

realizing dendrite-free, highly reversible, and highly stable Zn-metal-based electrodes. This nanoscale surface engineering maintained the benefits of the Zn electrode, such as the high energy density and high electrical conductivity of the Zn metal.

Finally, we examined the performance of the $Ti_{0.87}O_2$@Zn electrode as an anode for Zn-MnO_2 batteries. As shown in Figure S19, the $Ti_{0.87}O_2$@Zn anode exhibited a lower voltage plateau (1.51 V) in the charging process and a higher plateau (1.28 V) in the discharging process compared to the bare Zn anode (1.56 and 1.25 V, respectively). As a result, the $Ti_{0.87}O_2$@Zn anode delivered larger charge/discharge capacities (151 mAh g^{-1}/115 mAh g^{-1}) than the Zn anode (118 mAh g^{-1}/108 mAh g^{-1}). While the charge/discharge capacity was decreased as the charge current was increased for both, the $Ti_{0.87}O_2$@Zn anode exhibited a better rate performance than the Zn anode (Figure S20). These results verified that the $Ti_{0.87}O_2$@Zn anode is promising.

In summary, a 1 nm-thick monolayer film of $Ti_{0.87}O_2$ nanosheets was successfully deposited on a Zn sheet via spin coating to provide dendrite-free and reversible electrodes for zinc-based energy storage devices. The $Ti_{0.87}O_2$ nanosheets with negatively charged surfaces enabled effective adsorption, uniform redistribution, and enrichment of Zn^{2+} near the electrode. Thus, the overpotential for Zn nucleation was reduced and the H_2 evolution side reaction was suppressed, resulting in uniform Zn deposition. As a consequence, dendrite-free, reversible, and extremely stable electrodes were realized. Moreover, this molecularly thin interface preserved the high electrical conductivity of the Zn electrode, and largely improved the cycling stability of the Zn electrode from 105 to 1400 h at 1 mA cm^{-2}/1 mAh cm^{-2} without sacrificing energy density or cost. This work has presented a feasible interfacial engineering strategy for developing Zn electrodes with application promise. This approach will also be applicable to other metal electrodes, such as those of Li, Na, and Al metals.

ASSOCIATED CONTENT

Supporting Information. Preparation and characterization of layered titanate precursors and nanosheets, fabrication and characterization of the nanosheet-deposited electrodes, and the detailed experimental procedures.
This material is available free of charge via the Internet at http://pubs.acs.org.

AUTHOR INFORMATION

Corresponding Author

*Nobuyuki Sakai, Email: SAKAI.Nobuyuki@nims.go.jp
*Takayoshi Sasaki, Email: SASAKI.Takayoshi@nims.go.jp

Author Contributions

The manuscript was written through contributions of all authors. All authors have given approval to the final version of the manuscript. C.W. carried out the experiments involving materials fabrication, characterizations and electrochemical measurements, and wrote the original draft. N.S. carried out experiments on materials fabrication and characterization, and revised the manuscript. Y.E. carried out experiments on materials fabrication. D.T. carried out the microscopic observation of materials. R.M. revised the manuscript. T.S. conceived the experiments, supervised the project, and revised the manuscript. All authors discussed the results and commented on the manuscript.

Notes

The authors declare no competing financial interest.

ACKNOWLEDGMENT

The authors greatly acknowledge the support of the World Premier International Research Center Initiative (WPI), Ministry of Education, Culture, Sports, Science and Technology (MEXT), Japan, CREST of the Japan Science and Technology Agency (JST) (Grant No. JPMJCR17N1 & JPMJCR22B1), and Japan Society for the Promotion of Science (JSPS) (Grant No. P21036), Japan. The characterization of the cross-section profile was conducted with the help of Namiki Foundry in NIMS (1224, 20-270), and the surface state analysis was conducted with the help from the Materials Analysis Station in NIMS. The in-plane XRD measurement was performed under the approval of the Photon Factory Program Advisory Committee (Proposal No. 2020G503).

REFERENCES

(1) Larcher, D.; Tarascon, J-M. Towards greener and more sustainable batteries for electrical energy storage. *Nat. Chem.* **2015**, *7*, 19-29.

(2) Olabi, A. G.; Onumaegbu, C.; Wil-berforce, T.; Ramadan, M.; Abdelkareem, M. A.; Al – Alami, A. H. Critical review of energy storage systems. *Energy* **2021**, *214*, 118987.

(3) Dunn, B.; Kamath, H.; Tarascon, J-M. Electrical Energy Storage for the Grid: A Battery of Choices. *Science* **2011**, *334*, 928-935.

(4) Yang, Z.; Zhang, J.; Kintner-Meyer, M. C. W.; Lu, X.; Choi, D.; Lemmon, J. P.; Liu, J. Electrochemical Energy Storage for Green Grid. *Chem. Rev.* **2011**, *111*, 3577-3613.

(5) Ming, J.; Guo, J.; Xia, C.; Wang, W.; Alshareef, H. N. Zinc-ion batteries: Materials, mechanisms, and applications. *Mater. Sci. Eng., R* **2019**, *135*, 58-84.

(6) Song, M.; Tan, H.; Chao, D.; Fan, H. J. Recent Advances in Zn-Ion Batteries. *Adv. Funct. Mater.* **2018**, *28*, 1802564.

(7) Ma, L.; Schroeder, M. A.; Borodin, O.; Pollard, T. P.; Ding, M. S.; Wang, C.; Xu, K. Realizing high zinc reversibility in rechargeable batteries. *Nat. Energy* **2020**, *5*, 743-749.

(8) Li, C.; Xie, X.; Liang, S.; Zhou, J. Issues and Future Perspective on Zinc Metal Anode for Rechargeable Aqueous Zinc-ion Batteries. *Energy Environ. Mater.* **2020**, *3*, 146-159.

(9) Shin, J.; Lee, J.; Park, Y.; Choi, J. W. Aqueous zinc ion batteries: focus on zinc metal anodes. *Chem. Sci.* **2020**, *11*, 2028-2044.

(10) Ballesteros, J. C.; Díaz-Arista, P.; Meas, Y.; Ortega, R.; Trejo, G. Zinc electrodeposition in the presence of polyethylene glycol 20000. *Electrochim. Acta* **2007**, *52*, 3686-3696.

(11) Nayana, K. O.; Venkatesha, T. V.; Praveen, B. M.; Vathsala, K. Synergistic effect of additives on bright nanocrystalline zinc electrodeposition. *J. Appl. Electrochem.* **2011**, *41*, 39-49.

(12) Cao, J.; Zhang, D.; Gu, C.; Wang, X.; Wang, S.; Zhang, X.; Qin, J.; Wu, Z. S. Manipulating Crystallographic Orientation of Zinc Deposition for Dendrite-free Zinc Ion Batteries. *Adv. Energy Mater.* **2021**, *11*, 2101299.

(13) Hou, Z.; Gao, Y.; Tan, H.; Zhang, B. Realizing high-power and high-capacity zinc/sodium metal anodes through interfacial chemistry regulation. *Nat. Commun.* **2021**, *12*, 3083.

(14) Parker, J. F.; Chervin, C. N.; Pala, I. R.; Machler, M.; Burz, M. F.; Long, J. W.; Rolison, D. R. Rechargeable nickel-3D zinc

batteries: An energy-dense, safer alternative to lithium-ion. *Science* **2017**, *356*, 415-418.

(15) Zhang, Q.; Luan, J.; Fu, L.; Wu, S.; Tang, Y.; Ji, X.; Wang, H. The Three-Dimensional Dendrite-Free Zinc Anode on a Copper Mesh with a Zinc-Oriented Polyacrylamide Electrolyte Additive. *Angew. Chem. Int. Ed.* **2019**, *58*, 15841-15847.

(16) Wang, S. B.; Ran, Q.; Yao, R. Q.; Shi, H.; Wen, Z.; Zhao, M.; Lang, X. Y.; Jiang, Q. Lamella-nanostructured eutectic zinc-aluminum alloys as reversible and dendrite-free anodes for aqueous rechargeable batteries. *Nat. Commun.* **2020**, *11*, 1634.

(17) Wang, J.; Yang, Y.; Zhang, Y.; Li, Y.; Sun, R.; Wang, Z.; Wang, H. Strategies towards the challenges of zinc metal anode in rechargeable aqueous zinc ion batteries. *Energy Storage Mater.* **2021**, *35*, 19-46.

(18) He, H.; Qin, H.; Wu, J.; Chen, X.; Huang, R.; Shen, F.; Wu, Z.; Chen, G.; Yin, S.; Liu, J. Engineering Interfacial Layers to Enable Zn Metal Anodes for Aqueous Zinc-ion Batteries. *Energy Storage Mater.* **2021**, *43*, 317-336.

(19) Zhang, Q.; Luan, J.; Tang, Y.; Ji, X.; Wang, H. Interfacial Design of Dendrite-Free Zinc Anodes for Aqueous Zinc-Ion Batteries. *Angew. Chem. Int. Ed.* **2020**, *59*, 13180-13191.

(20) Kang, L.; Cui, M.; Jiang, F.; Gao, Y.; Luo, H.; Liu, J.; Liang, W.; Zhi, C. Nanoporous $CaCO_3$ Coatings Enabled Uniform Zn Stripping/Plating for Long-Life Zinc Rechargeable Aqueous Batteries. *Adv. Energy Mater.* **2018**, *8*, 1801090.

(21) Zhang, Q.; Luan, J.; Huang, X.; Wang, Q.; Sun, D.; Tang, Y.; Ji, X.; Wang, H. Revealing the role of crystal orientation of protective layers for stable zinc anode. *Nat. Commun.* **2020**, *11*, 3961.

(22) Liang, P.; Yi, J.; Liu, X.; Wu, K.; Wang, Z.; Cui, J.; Liu, Y.; Wang, Y.; Xia, Y.; Zhang, J. Highly Reversible Zn Anode Enabled by Controllable Formation of Nucleation Sites for Zn-Based Batteries. *Adv. Funct. Mater.* **2020**, *30*, 1908528.

(23) Liu, M.; Cai, J.; Ao, H.; Hou, Z.; Zhu, Y.; Qian, Y. Na-$Ti_2(PO_4)_3$ Solid-State Electrolyte Protection Layer on Zn Metal Anode for Superior Long-Life Aqueous Zinc-Ion Batteries. *Adv. Funct. Mater.* **2020**, *30*, 2004885.

(24) Yan, H.; Li, S.; Nan, Y.; Yang, S.; Li, B. Ultrafast Zinc-Ion-Conductor Interface toward High-Rate and Stable Zinc Metal Batteries. *Adv. Energy Mater.* **2021**, *11*, 2100186.

(25) Li, T. C.; Lim, Y. V.; Xie, X.; Li, X. L.; Li, G.; Fang, D.; Li, Y.; Ang, Y. S.; Ang, L. K.; Yang, H. Y. ZnSe Modified Zinc Metal Anodes: Toward Enhanced Zincophilicity and Ionic Diffusion. *Small* **2021**, *17*, 2101728.

(26) Hao, J.; Li, X.; Zhang, S.; Yang, F.; Zeng, X.; Zhang, S.; Bo, G.; Wang, C.; Guo, Z. Designing Dendrite-Free Zinc Anodes for Advanced Aqueous Zinc Batteries. *Adv. Funct. Mater.* **2020**, *30*, 2001263.

(27) Zhao, Z.; Zhao, J.; Hu, Z.; Li, J.; Li, J.; Zhang, Y.; Wang, C.; Cui, G. Long-life and deeply rechargeable aqueous Zn anodes enabled by a multifunctional brightener-inspired interphase. *Energy Environ. Sci.* **2019**, *12*, 1938-1949.

(28) Liu, X.; Yang, F.; Xu, W.; Zeng, Y.; He, J.; Lu, X. Zeolitic Imidazolate Frameworks as Zn^{2+} Modulation Layers to Enable Dendrite-Free Zn Anodes. *Adv. Sci.* **2020**, *7*, 2002173.

(29) Yuksel, R.; Buyukcakir, O.; Seong, W. K.; Ruoff, R. S. Metal-Organic Framework Integrated Anodes for Aqueous Zinc-Ion Batteries. *Adv. Energy Mater.* **2020**, *10*, 1904215.

(30) He, H.; Liu, J. Suppressing Zn dendrite growth by molecular layer deposition to enable long-life and deeply rechargeable aqueous Zn anodes. *J. Mater. Chem. A* **2020**, *8*, 22100-22110.

(31) Cui, J.; Li, Z.; Xu, A.; Li, J.; Shao, M. Confinement of Zinc Salt in Ultrathin Heterogeneous Film to Stabilize Zinc Metal Anode. *Small* **2021**, *17*, 2100722.

(32) Liu, M.; Yang, L.; Liu, H.; Amine, A.; Zhao, Q.; Song, Y.; Yang, J.; Wang, K.; Pan, F. Artificial Solid-Electrolyte Interface Facilitating Dendrite-Free Zinc Metal Anodes via Nanowetting Effect. *ACS Appl. Mater. Interfaces* **2019**, *11*, 32046-32051.

(33) Zhao, K.; Wang, C.; Yu, Y.; Yan, M.; Wei, Q.; He, P.; Dong, Y.; Zhang, Z.; Wang, X.; Mai, L. Ultrathin Surface Coating Enables Stabilized Zinc Metal Anode. *Adv. Mater. Interfaces* **2018**, *5*, 1800848.

(34) Hu, L.; Ma, R.; Ozawa, T. C.; Sasaki, T. Oriented Monolayer Film of Gd_2O_3:0.05Eu Crystallites: Quasi-Topotactic Transformation of the Hydroxide Film and Drastic Enhancement of Photoluminescence Properties. *Angew. Chem. Int. Ed.* **2009**, *48*, 3846-3849.

(35) Taniguchi, T.; Nurdiwijayanto, L.; Li, S.; Lim, H. E.; Miyata, Y.; Lu, X.; Ma, R.; Tang, D.-M.; Ueda, S.; Tsukagoshi, K.; Sasaki, T.; Osada, M. On/Off Boundary of Photocatalytic Activity between Single- and Bilayer MoS_2. *ACS Nano* **2020**, *14*, 6663-6672.

(36) He, Y.; Jia, L.; Lu, X.; Wang, C.; Liu, X.; Chen, G.; Wu, D.; Wen, Z.; Zhang, N.; Yamauchi, Y.; Sasaki, T.; Ma, R. Molecular-Scale Manipulation of Layer Sequence in Heteroassembled Nanosheet Films toward Oxygen Evolution Electrocatalysts. *ACS Nano* **2022**, *16*, 4028-4040.

(37) Zhang, G.; Zhang, Y.-W. Thermal properties of two-dimensional materials. *Chin. Phys. B* **2017**, *26*, 034401.

(38) Cheng, L.; Wang, X.; Gong, F.; Liu, T.; Liu, Z. 2D Nanomaterials for Cancer Theranostic Applications. *Adv. Mater.* **2020**, *32*, 1902333.

(39) Dong, X.; Osada, M.; Ueda, H.; Ebina, Y.; Kotani, Y.; Ono, K.; Ueda, S.; Kobayashi, K.; Takada, K.; Sasaki, T. Synthesis of Mn-Substituted Titania Nanosheets and Ferromagnetic Thin Films with Controlled Doping. *Chem. Mater.* **2009**, *21*, 4366-4373.

(40) Wang, X.; Li, X.; Aya, S.; Araoka, F.; Ishida, Y.; Kikkawa, A.; Kriener, M.; Taguchi, Y.; Ebina, Y.; Sasaki, T.; Koshiya, S.; Kimoto, K.; Aida, T. Reversible Switching of the Magnetic Orientation of Titanate Nanosheets by Photochemical Reduction and Autoxidation. *J. Am. Chem. Soc.* **2018**, *140*, 16396-16401.

(41) Ma, R.; Sasaki, T. Nanosheets of Oxides and Hydroxides: Ultimate 2D Charge-Bearing Functional Crystallites. *Adv. Mater.* **2010**, *22*, 5082-5104.

(42) Osada, M.; Sasaki, T. Two-Dimensional Dielectric Nanosheets: Novel Nanoelectronics From Nanocrystal Building Blocks. *Adv. Mater.* **2012**, *24*, 210-228.

(43) Wang, L.; Sasaki, T. Titanium Oxide Nanosheets: Graphene Analogues with Versatile Functionalities. *Chem. Rev.* **2014**, *114*, 9455-9486.

(44) Ma, R.; Sasaki, T. Two-Dimensional Oxide and Hydroxide Nanosheets: Controllable High-Quality Exfoliation, Molecular Assembly, and Exploration of Functionality. *Acc. Chem. Res.* **2015**, *48*, 136-143.

(45) Taniguchi, T.; Nurdiwijayanto, L.; Ma, R.; Sasaki, T. Chemically exfoliated inorganic nanosheets for nanoelectronics. *Appl. Phys. Rev.* **2022**, *9*, 021313.

(46) Li, B.-W.; Osada, M.; Ozawa, T. C.; Ebina, Y.; Akatsuka, K.; Ma, R.; Funakubo, H.; Sasaki, T. Engineered Interfaces of Artificial Perovskite Oxide Superlattices via Nanosheet Deposition Process. *ACS Nano* **2010**, *4*, 6673-6680.

(47) Akatsuka, K.; Haga, M.; Ebina, Y.; Osada, M.; Fukuda, K.; Sasaki, T. Construction of Highly Ordered Lamellar Nanostructures through Langmuir−Blodgett Deposition of Molecularly Thin Titania Nanosheets Tens of Micrometers Wide and Their Excellent Dielectric Properties. *ACS Nano* **2009**, *3*, 1097-1106.

(48) Keller, S. W.; Kim, H.-N.; Mallouk, T. E. Layer-by-Layer Assembly of Intercalation Compounds and Heterostructures on Surfaces: Toward Molecular "Beaker" Epitaxy. *J. Am. Chem. Soc.* **1994**, *116*, 8817-8818.

(49) Schaaki, R. E.; Mallouk, T. E. Perovskites by Design: A Toolbox of Solid-State Reactions. *Chem. Mater.* **2002**, *14*, 1455-1471.

(50) Sasaki, T.; Ebina, Y.; Tanaka, T.; Harada, M.; Watanabe, M.; Decher, G. Lay-er-by-Layer Assembly of Titania Nanosheet/Polycation Composite Films. *Chem. Mater.* **2001**, *13*, 4661-4667.

(51) Matsuba, K.; Wang, C.; Saruwatari, K.; Uesusuki, Y.; Akatsuka, K.; Osada, M.; Ebina, Y.; Ma, R.; Sasaki, T. Neat mono-

layer tiling of molecularly thin two-dimensional materials in 1 min. *Sci. Adv.* **2017**, *3*, 1700414.

(52) Yano, H.; Sakai, N.; Ebina, Y.; Ma, R.; Osada, M.; Fujimoto, K.; Sasaki, T. Construction of Multilayer Films and Superlattice- and Mosaic-like Heterostructures of 2D Metal Oxide Nanosheets via a Facile Spin-Coating Process. *ACS Appl. Mater. Interfaces* **2021**, *13*, 43258-43265.

(53) Sakai, N.; Sasaki, T. Guidelines for Arranging 2D Nanosheets into Neatly Tiled Monolayer Films by a Spin-Coating Process. *Langmuir* **2022**, *38*, 12399-12407.

(54) Shi, Y.; Osada, M.; Ebina, Y.; Sasaki, T. Single Droplet Assembly for Two-Dimensional Nanosheet Tiling. *ACS Nano* **2020**, *14*, 15216-15226.

(55) Momma, K.; Izumi, F., VESTA 3 for Three-Dimensional Visualization of Crystal, Volumetric and Morphology Data. *J. Appl. Crystallogr.* **2011**, *44*, 1272-1276.

(56) Sasaki, T.; Watanabe, M.; Hashizume, H.; Yamada, H.; Nakazawa, H. Macromolecule-like Aspects for a Colloidal Suspension of an Exfoliated Titanate. Pairwise Association of Nanosheets and Dynamic Reassembling Process Initiated from It. *J. Am. Chem. Soc.* **1996**, *118*, 8329-8335.

(57) Sasaki, T.; Watanabe, M. Osmotic Swelling to Exfoliation. Exceptionally High Degrees of Hydration of a Layered Titanate. *J. Am. Chem. Soc.* **1998**, *120*, 4682-4689.

(58) Maluangnont, T.; Matsuba, K.; Geng, F.; Ma, R.; Yamauchi, Y.; Sasaki, T. Osmotic Swelling of Layered Compounds as a Route to Producing High-Quality Two-Dimensional Materials. A Comparative Study of Tetra-methylammonium versus Tetrabutylammonium Cation in a Lepidocrocite-type Titanate. *Chem. Mater.* **2013**, *25*, 3137-3146.

(59) Sasaki, T.; Ebina, Y.; Kitami, Y.; Watanabe, M. Two-Dimensional Diffraction of Molecular Nanosheet Crystallites of Titanium Oxide. *J. Phys. Chem. B* **2001**, *105*, 6116-6121.

(60) Xiong, P.; Zhang, F.; Zhang, X.; Liu, Y.; Wu, Y.; Wang, S.; Safaei, J.; Sun, B.; Ma, R.; Liu, Z.; Bando, Y.; Sasaki, T.; Wang, X.; Zhu, J.; Wang, G. Atomic-scale regulation of anionic and cationic migration in alkali metal batteries. *Nat. Commun.* **2021**, *12*, 4184.

(61) Sakai, N.; Fukuda, K.; Shibata, T.; Ebina, Y.; Takada, K.; Sasaki, T. Photoinduced Hydrophilic Conversion Properties of Titania Nanosheets. *J. Phys. Chem. B* **2006**, *110*, 6198-6203.

(62) Shibata, T.; Sakai, N.; Fukuda, K.; Ebina, Y.; Sasaki, T. Photocatalytic properties of titania nanostructured films fabricated from titania nanosheets. *Phys. Chem. Chem. Phys.* **2007**, *9*, 2413-2420.

Table of Contents